Nonlinear MHD Analysis for LHD Plasmas

K. Ichiguchi 1), N.Nakajima 1), M. Wakatani 2), B.A. Carreras 3)

1) National Institute for Fusion Science, Oroshi-cho 322-6, Toki, 509-5292, Japan
2) Graduate School of Energy Science, Kyoto University, Gokasho, Uji, 611-0011, Japan
3) Oak Ridge National Laboratory, Oak Ridge, Tennessee 37831, USA

e-mail contact of main author: ichiguch@nifs.ac.jp

Abstract. The nonlinear behavior of the interchange modes with multi-helicity in the Large Helical Device is analyzed based on the reduced MHD equations. In the equilibrium at sufficiently low beta value, the saturation of a single mode and the following excitation of other single mode whose resonant surface is close to that of the saturated mode are slowly repeated. This sequence leads to the local deformation of the pressure profile. Increasing the beta value with the pressure profile fixed, a bursting phenomenon due to the overlap of multiple modes is observed in the kinetic energy, which results in the global reduction of the pressure profile. Increasing the beta value using the pressure profile saturated at the lower beta value suppresses the bursting behavior. This result indicates the possibility that the pressure profile is self-organized so that the LHD plasma should attain the high beta regime through a stable path.

1. Introduction

In the recent experiments in the Large Helical Device (LHD), high performance discharges have been successfully carried out in the configuration with the inward shift of the vacuum magnetic axis. Particularly, in the high beta discharges, the average beta value of 3.2% was achieved in the configuration with the vacuum magnetic axis located at $R_{ax} = 3.6$m[1]. On the other hand, the linear MHD stability of the plasmas was studied with the RESORM code[2] which is based on the reduced MHD equations for stellarator configurations. The initial stability studies[3] were done using smooth pressure profiles. The results of these studies showed that low-n ideal interchange modes are unstable for beta values lower than the experimental ones. Here, n denotes the toroidal mode number.

To explain the discrepancy between theory and experiment it is necessary to invoke the existence of a stabilizing mechanism. Because the ideal interchange modes are driven by the pressure gradient, one possible stabilizing mechanism is the local flattening of the pressure profile at the low order resonant surfaces[4,5]. It was shown by iterating the equilibrium and the linear stability calculations that staircase-like profile of the pressure can effectively stabilize the multiple modes with different n simultaneously. However, it was not clarified whether such locally flat profile can be actually achieved in the toroidal geometry. Besides, the overlap of the modes whose resonant surfaces are radially close to each other possibly becomes a critical issue. In order to study these problems, nonlinear analysis is inevitable. Thus, in this paper, we discuss the nonlinear behavior of the MHD fluctuation in the LHD plasmas, especially in the point of the the pressure profile variation.

2. Basic Equations and Numerical Scheme

We have developed a nonlinear MHD calculation code extending the RESORM code, which solves the reduced MHD equations based on the modified stellarator ordering including the

higher order toroidal effect[6]. The equations are Ohm's law, vorticity equation, and the equation of state. These equations can be written in terms of the poloidal magnetic flux, Ψ, the velocity stream function, Φ, and the plasma pressure, P. These equations are:

$$\frac{\partial \Psi}{\partial t} = -\left(\frac{R}{R_0}\right)^2 \mathbf{B}\cdot\nabla\Phi + \frac{1}{S}J_\zeta, \tag{1}$$

$$\frac{dU}{dt} = \left(\frac{R}{R_0}\right)^2 \left(-\mathbf{B}\cdot\nabla J_\zeta + \frac{\beta_0}{2\varepsilon^2}\nabla\Omega\times\nabla P\cdot\nabla\zeta\right) + \nu\hat{\nabla}_\perp^2 U, \tag{2}$$

and

$$\frac{dP}{dt} = \kappa_\perp \Delta_* P + \varepsilon^2 \kappa_\parallel \left(\frac{R}{R_0}\right)^2 \mathbf{B}\cdot\nabla(\mathbf{B}\cdot\nabla P). \tag{3}$$

Here, ζ denotes the toroidal angle and $\nabla_\perp$ is defined as $\nabla_\perp = \nabla - \nabla\zeta(\partial/\partial\zeta)$. The magnetic differential operator and the convective time derivative are given by

$$\mathbf{B}\cdot\nabla = g\left(\frac{R_0}{R}\right)^2 \frac{\partial}{\partial\zeta} - \nabla\Psi\times\nabla\zeta\cdot\nabla \tag{4}$$

and

$$\frac{d}{dt} = \frac{\partial}{\partial t} + \mathbf{v}_\perp\cdot\nabla, \quad \mathbf{v}_\perp = \left(\frac{R}{R_0}\right)^2 \nabla\Phi\times\nabla\zeta, \tag{5}$$

respectively. The factor g implies the diamagnetic effect in the toroidal field. The term of $\nabla\Omega$ means the averaged magnetic curvature driving the interchange mode and Ω is given by

$$\Omega = \frac{1}{2\pi}\int_0^{2\pi} d\zeta \left(\frac{R}{R_0}\right)^2 \left(1 + \frac{|\mathbf{B}_{eq} - \overline{\mathbf{B}_{eq}}|^2}{B_0^2}\right), \tag{6}$$

where the subscript 'eq' means the equilibrium quantity and the overline denotes the toroidally averaged value. The vorticity U and the toroidal current density J_ζ are expressed by

$$U = \hat{\nabla}_\perp^2\Phi = \left(\frac{R}{R_0}\right)^2 \nabla\cdot\nabla_\perp\Phi, \quad \text{and} \quad J_\zeta = \Delta_*\Psi = \left(\frac{R}{R_0}\right)^2 \nabla\cdot\left(\frac{R_0}{R}\right)^2 \nabla_\perp\Psi, \tag{7}$$

respectively. The magnetic field is normalized to its value at the magnetic axis, B_0, and β_0 denotes the beta value at the axis. The lengths in the ζ and the perpendicular directions are normalized by the major radius R_0 and the average minor radius a of the plasma, respectively, and ε is given by a/R_0. The time is normalized by the poloidal Alfvén time τ_A defined by $R_0\sqrt{\mu_0\rho_m}/B_0$, where ρ_m and μ_0 are the mass density and the vacuum permeability, respectively. The magnetic Reynolds number S is defined by $S = \tau_R/\tau_A$, where $\tau_R = \mu_0 a^2/\eta$ is the resistive diffusion time and η denotes the resistivity. The resistivity is assumed to be constant in the present work. We introduce the viscosity for the perpendicular flow in the vorticity equation. The coefficient ν is normalized by $a^2\rho_m/\tau_A$. The perpendicular and parallel heat conductivity terms are also introduced in the equation of state with the coefficients of $\kappa_\perp$ and $\kappa_\parallel$, respectively, which are normalized by a^2/τ_A. In the resistivity and the heat conductivity terms , only the perturbed parts of J_ζ and P are included, respectively.

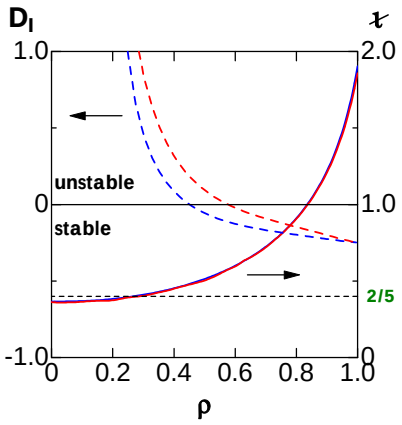

FIG.1. Profiles of Mercier quantity normalized so that the shear term should be -1/4 (dashed lines) and rotational transform (solid lines) for the pressure profile of eq.(8) at $\beta_0 = 0.5\%$ (blue) and 1.0% (red). Rational surface with $\iota = 2/5$ is indicated.

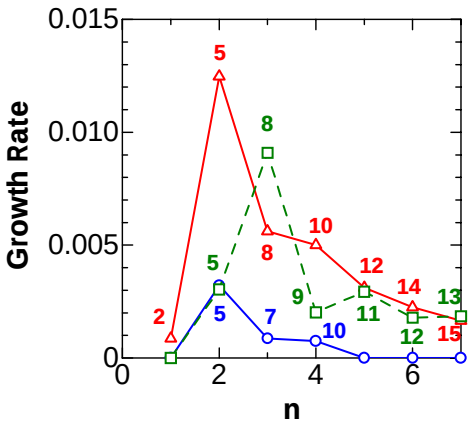

FIG.2. Linear growth rates versus toroidal mode number n. Circles and triangles show the growth rates for the pressure of eq.(8) at $\beta_0 = 0.5\%$ and 1.0%, respectively. Squares show the growth rates at $\beta_0 = 1.0\%$ for the pressure profile saturated nonlinearly at $\beta_0 = 0.5\%$. Numbers indicate the dominant poloidal mode number of each n mode.

The flux coordinates (ρ, θ, ζ) are employed to simplify the magnetic differential operator. Here ρ and θ are the square root of the normalized toroidal flux and the poloidal angle, respectively. The finite difference is employed for the radial discretization. The radial grid number used here is 192. The dependence of the poloidal and the toroidal angles are expressed by the Fourier series. The multi-helicity components of the perturbations are treated. The mode coupling is calculated through the direct convolution of the Fourier coefficients. For the time evolution, the two-step explicit algorithm[7] is employed, while only the linear dissipation operators are treated implicitly in each step. This code examines three-dimensional static equilibrium which is calculated by using the VMEC code[8]. The toroidally averaged geometry is used in the construction of the flux coordinates. Therefore, the toroidal effects are included automatically. The equilibrium toroidal current density is calculated by using the averaged equilibrium equation with the averaged curvature given by eq.(6).

2. Equilibrium and Linear Stability

First, we consider zero current equilibria for the shifted-in LHD configuration ($R_{ax} = 3.6$m) using the pressure profile of the form

$$P = P_0(1-\rho^2)(1-\rho^8). \tag{8}$$

In the equilibrium calculation, the free boundary condition is employed with the constraint that the separatrix plays a role of a virtual limiter at $R = 4.63$m[9]. The pressure profile of eq.(8) is close to the one observed in the experiments for $\langle\beta\rangle < 1\%$[10], where $\langle\beta\rangle$ denotes the volume average beta. Here we focus on the equilibria at $\beta_0 = 0.5\%$ and 1.0%, which correspond to $\langle\beta\rangle = 0.21\%$ and 0.43%, respectively. Figure 1 shows the profiles of the rotational transform and the Mercier quantity D_I[11]. The difference in the rotational transform between the equilibria is quite small. The equilibrium is Mercier unstable in the regions of $\rho < 0.44$ and $\rho < 0.57$ at $\beta_0 = 0.5\%$ and 1.0%, respectively, because of the low shear and high magnetic hill. For the

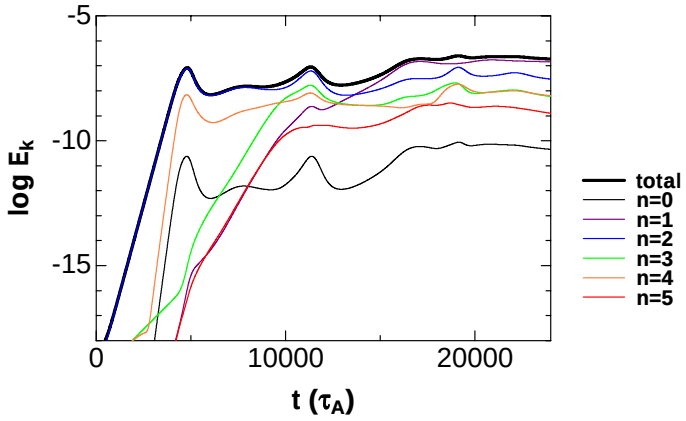

FIG.3. Time evolution of the kinetic energy of the perturbation for the $\beta_0 = 0.5\%$ equilibrium. Thick line shows the total energy and thin lines show the $n = 0$, 1, 2, 3, 4 and 5 components.

nonlinear analysis, we use the dissipation parameters of $S = 10^6$, $\nu = 10^{-4}$, $\kappa_\perp = 10^{-6}$ and $\varepsilon^2\kappa_\parallel = 10^{-2}$ ($\varepsilon = 0.16$). The linear growth rates with these parameters at $\beta_0 = 0.5\%$ and 1.0% are shown in Fig.2 as the function of the toroidal mode number n. All unstable modes have typical interchange mode structure. Only the modes with $n = 2$, 3 and 4 are linearly unstable at $\beta_0 = 0.5\%$, while all of the modes for $1 \le n \le 7$ are unstable at $\beta_0 = 1.0\%$ and the growth rates are much larger than those at 0.5%. In each equilibrium, the $n = 2$ mode has the largest growth rate and the $m = 5$ is the dominant component in this mode.

3. Mild Saturation with Local Pressure Flattening

For the nonlinear calculation with $\beta_0 = 0.5\%$, we use the following range of Fourier components: $0 \le n \le 5$ and $0 \le m \le 16$, where m denotes the poloidal mode number. Figure 3 shows time evolution of the kinetic energy of the perturbation which is defined by $E_k = \sum_n E_k^n$, $E_k^n = \frac{1}{2}\int |\nabla_\perp \sum_m \Phi_{mn} \sin(m\theta - n\zeta)|^2 dV$.

The linear phase is dominated by the $(m,n) = (5,2)$ mode, which is nonlinearly saturated at $t = 4800\tau_A$. In the nonlinear phase, the variation of the kinetic energy is small and slow. Figure 4 shows the flow pattern and the pressure contour at $t = 4800\tau_A$. The convective flow forms the vortices around the resonant surface with $\iota = 2/5$. The number of the vortices is two times of the poloidal mode number. These vortices interchange the high and the low pressure regions alternatively in the poloidal direction. Therefore, the structure like a mushroom is generated. As a result, the average pressure, $\langle P \rangle = \tilde{P}_{m=0,n=0} + P_{eq}$, is locally flattened around the rational surface as shown in Fig. 5, where the tilde means the perturbed quantity. On the other hand, it is obtained that the compression of the magnetic surface due to the vortices causes the driven reconnection of the field line. Because the island is located at the vortex position, the number is also two times of the poloidal mode number like the case in Ref.[12].

The local pressure flattening makes the pressure gradient steep at the both sides of the flat region. Then, the mode resonant at the region with the steepened pressure gradient can be destabilized. In the saturation of the $(m,n) = (5,2)$ mode, the pressure gradient at the surface with $\iota = 3/7$ is steepened, which is located just outside the $\iota = 2/5$ surface. Then, the $(m,n) = (7,3)$ mode grows, and saturates at $t = 11325\tau_A$, as shown in Fig.3. As shown in Fig.5, two flat pressure

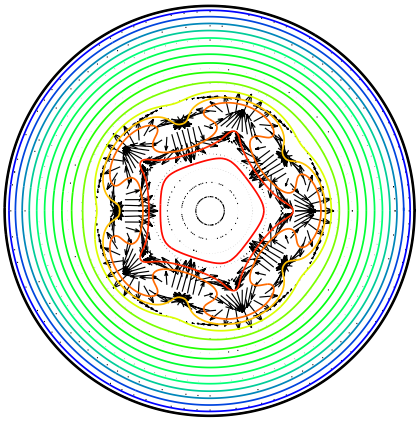

FIG.4. Flow pattern (black arrows) and pressure contour on the (ρ,θ) plane at $\zeta=0$ cross section at $t=4800\tau_A$ for the $\beta_0=0.5\%$ equilibrium, plotted only in the region of $\rho\leq 0.6$. Color of the pressure contour varies red to blue as the value decreases. The longest arrow corresponds to the largest velocity in this plane.

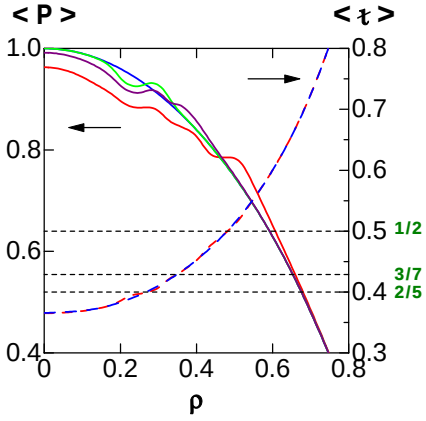

FIG.5. Profiles of average pressure $\langle P\rangle$ (solid lines) at $t=0$(blue), $4800\tau_A$(green), $11325\tau_A$(purple) and $24000\tau_A$(red) and average rotational transform $\langle\iota\rangle$ (dashed lines) at $t=0$(blue) and $24000\tau_A$(red) in the region of $\rho\leq 0.8$ for the $\beta_0=0.5\%$ equilibrium. Average pressure is normalized so that $\langle P\rangle(\rho=0,t=0)$ should be unity. Rational surfaces with $\iota=2/5$, 3/7 and 1/2 are indicated.

regions coexist at this time. The saturation of the $(m,n)=(7,3)$ mode makes the gradient at $\iota=1/2$ surface steep in turn, and excites the $(m,n)=(2,1)$ mode. All modes are saturated completely at $t=24000\tau_A$. The average pressure profile is deformed so as to be the staircase-like shape with multiple flat regions, as shown in Fig.5. The average rotational transform defined by $\langle\iota\rangle=\frac{1}{\rho}\frac{\partial\tilde{\Psi}_{m=0,n=0}}{\partial\rho}+\iota_{eq}$ is also plotted in Fig.5. The nonlinear effect on the average rotational transform is much weaker than on the pressure. Note that the $n=1$ mode is dominant in the kinetic energy at $t=24000\tau_A$, which is linearly stable.

4. Global Pressure Reduction due to Bursting Activity

Next, we examine the nonlinear evolution of the perturbation for $\beta_0=1.0\%$. The calculation is carried out in the Fourier space of $0\leq n\leq 7$ and $0\leq m\leq 22$. Figure 6 shows the time evolution of the kinetic energy. The $(m,n)=(5,2)$ component is dominant in the linear phase as in the case of $\beta_0=0.5\%$. However, a bursting activity appears after the dominant linear mode saturates. In the bursting phase, the multiple modes with different helicity grow and decay rapidly. The kinetic energy of each mode for $n\geq 1$ is in the level of $E_k^n\geq 10^{-7}$. This fluctuation level is almost one-order larger than that in the case of $\beta_0=0.5\%$. This implies that the driving force for each mode is enhanced. Figure 7 shows the flow pattern and the pressure contour at $t=3840\tau_A$ where E_k has a maximum value. The pressure structure is too complicated to identify the mode number although the $n=2$ mode is dominant in the kinetic energy at this time. The property of the pressure structure indicates the overlaps of many components in the bursting phase. This is due to the enhancement of the mode width by the large driving force.

The profile of the average pressure shows the several flat regions corresponding to $\iota=2/5$, 4/9, 1/2 and 4/7 at $t=3840\tau_A$, as shown in Fig.8. Particularly, there exist large flat pressure regions around the $\iota=2/5$ and the $\iota=1/2$ surfaces. The regions with strongly steep pressure gradient are

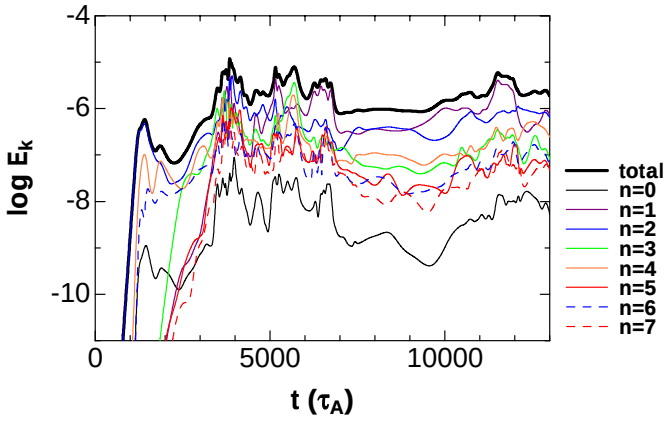

FIG.6. Time evolution of the kinetic energy of the perturbation for the $\beta_0 = 1.0\%$ equilibrium with the pressure of eq.(8). Thick line shows the total energy and thin lines show the $n = 0$, 1, 2, 3, 4, 5, 6 and 7 components.

located just outside the large flat pressure regions. It can be considered that such structure in the average pressure results from the cooperative flow of the overlapped modes. After the bursting phenomena, a large amount of the pressure in the core region is transported to the peripheral region. The central pressure decreases to 90% of the initial value and the whole gradient is also reduced in the region of $\rho \leq 0.5$ at $t = 13000\tau_A$ as shown in Fig.8. Thus, the bursting activity causes the global reduction in the pressure.

5. Stable Path to High Beta Regime

For pressure profile in eq.(8), the results in the previous section indicate that the achievable beta value in LHD may be limited by the bursting activity. On the other hand, as the beta value increases we expect a succession of pressure profiles that vary continuously with the beta. In order to simulate this situation, we utilize the saturated pressure profile at $\beta_0 = 0.5\%$ for the calculation at $\beta_0 = 1.0\%$ here, instead of the profile of eq.(8). The initial profile is determined by taking the average profile at $t = 24000\tau_A$ at $\beta_0 = 0.5\%$ and increasing the beta value up to 1.0%. Then, the three-dimensional equilibrium is calculated with the VMEC code under the free-boundary condition to include the beta dependence of the plasma boundary.

The linear growth rates for this equilibrium are plotted in Fig.2. The dominant mode is the $n = 3$ mode, and the growth rates are reduced for other modes compared with those in the equilibrium with eq.(8). The nonlinear evolution of the kinetic energy is shown in Fig.9. The behavior is similar to that in the $\beta_0 = 0.5\%$ case. The saturation of the $(m,n) = (8,3)$ mode at $t = 1700\tau_A$ slowly excites the $(m,n) = (5,2)$ mode. The saturation of the (5,2) mode occurs at $t = 3000\tau_A$, which excites the $(m,n) = (7,3)$ and (8,3) modes. After the sequence, the variation of the kinetic energy is small and slow. No bursting phenomenon appears in the time range of $t \leq 13000\tau_A$. This is because the driving forces of the $n = 1$, 2 and 4 modes are already reduced by the deformation of the initial pressure profile. New flat regions are generated around $\iota = 2/3$ and 6/11 in the average pressure profile at $t = 13000\tau_A$, as shown in Fig.10. However, they are just the local variations and the reduction of the core pressure is much smaller than that of the bursting case. Thus, the plasma pressure can be self-organized so as to suppress the bursting activity in the increase of the beta value from $\beta_0 = 0.5\%$ to 1.0%.

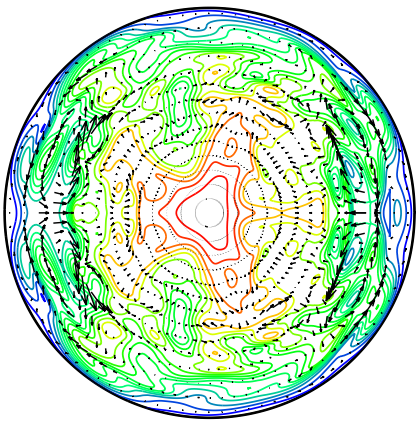

FIG.7. Flow pattern (black arrows) and pressure contour on the (ρ,θ) plane at $\zeta = 0$ cross section at $t = 3840\tau_A$ for the $\beta_0 = 1.0\%$ equilibrium with the pressure eq.(8), plotted only in the region of $\rho \leq 0.6$. Color of the pressure contour varies red to blue as the value decreases. The longest arrow corresponds to the largest velocity in this plane.

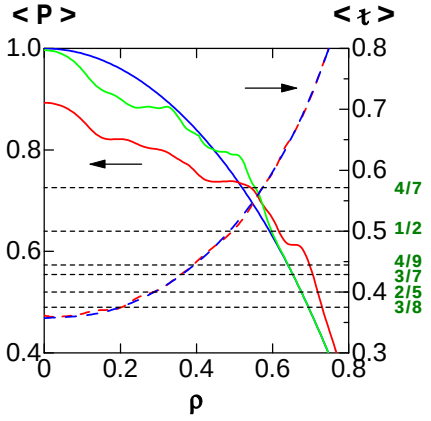

FIG.8. Profiles of average pressure $\langle P \rangle$ (solid lines) at $t = 0$(blue), $3840\tau_A$(green), and $13000\tau_A$(red) and average rotational transform $\langle \iota \rangle$ (dashed lines) at $t = 0$(blue) and $13000\tau_A$(red) in the region of $\rho \leq 0.8$ for the $\beta_0 = 1.0\%$ equilibrium with the pressure eq.(8). Rational surfaces with $\iota = 3/8, 2/5, 3/7, 4/9, 1/2$ and $4/7$ are indicated.

6. Conclusions

The nonlinear evolution of the interchange mode with multi-helicity is examined in the inward-shifted low-beta LHD equilibria with almost parabolic pressure profile. The behavior is different depending on the beta value. In the case of the sufficiently low beta value, the perturbations are slowly saturated in the low fluctuation level. The local pressure flattening due to the saturation of a single mode steepens the pressure gradient outside the flat region, and excites other single mode resonant at the steep gradient region. Therefore, the saturation and the excitation of the modes with different helicity are succeeded alternatively in the time evolution. The resultant pressure profile is staircase-like, as is expected by the linear calculation[4]. The occurrence of such mild saturation is attributed to the fact that only a few modes with different helicity are destabilized and the driving force of each mode is weak. In this case, the distance between the resonant surfaces of the unstable modes is wide enough for each mode to generate the flat pressure region needed for the saturation. Thus, the variation in the pressure profile is limited in the local regions.

On the other hand, increasing the beta value with the pressure profile fixed enhances the driving force. Then, the number of the unstable mode increases and the larger width of the flat pressure region is needed for the saturation of each mode. If the distance between the resonant surfaces of the unstable modes is smaller than the width of the necessary flat region for the saturation of the modes, the modes can overlap each other and the bursting activity is observed in the kinetic energy. Because the multiple modes grow and overlap in the core region for $\rho \leq 0.5$ in the present case for $\beta_0 = 1.0\%$, the bursting activity continues until the pressure gradient is decreased all over the region. Thus, the global reduction of the pressure profile is caused.

We simulate the continuous change of the pressure profile in the increase of the beta value by employing the saturated pressure profile at the lower beta value. It is demonstrated that the

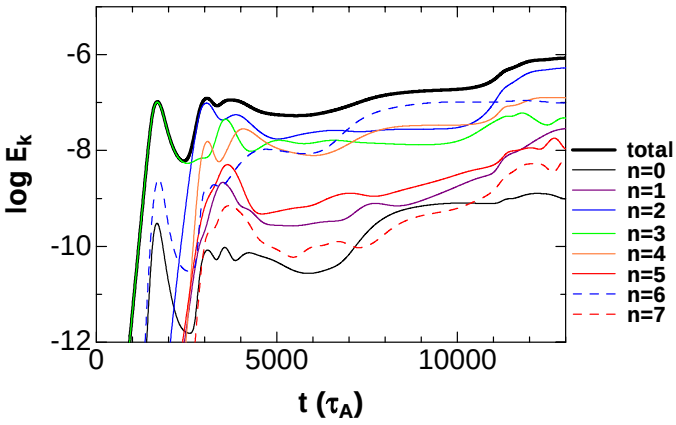

FIG.9. Time evolution of the kinetic energy of the perturbation for the $\beta_0 = 1.0\%$ equilibrium with the saturated pressure profile at $\beta_0 = 0.5\%$. Thick line shows the total energy and thin lines show the $n = 0$, 1, 2, 3, 4, 5, 6 and 7 components.

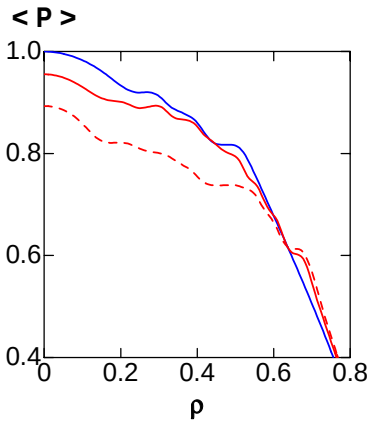

FIG.10. Profiles of average pressure $\langle P \rangle$ (solid lines) at $t = 0$(blue) and $13000\tau_A$(red) in the region of $\rho \leq 0.8$ for the $\beta_0 = 1.0\%$ equilibrium with the saturated pressure profile at $\beta_0 = 0.5\%$. Profile of the average pressure at $t = 13000\tau_A$ in Fig.8 is also shown by dashed red line for the comparison.

modes are nonlinearly saturated slowly as in the lower beta case. The bursting activity, which may limit the achievable beta value, is avoided by the reduction of the driving force due to the local deformation of the initial pressure profile. This result indicates the possibility that the pressure profile is self-organized through the nonlinear evolution of the interchange mode in LHD so that the plasma should attain the high beta regime beyond the linear stability limit for the fixed smooth pressure profiles.

Acknowledgment

This work was partially supported by the Grant-in-Aid for Scientific Research (C) of the Ministry of Education, Culture, Sports, Science and Technology, Japan.

References

[1] MOTOJIMA, O., et al., "Recent Advance in LHD Experiment", this conference, paper OV/1-6.
[2] ICHIGUCHI, K., et al., Nucl. Fusion **29** (1989) 2093.
[3] ICHIGUCHI, K., "Ideal and Resistive Stability of Free-Boundary LHD Equilibria" (Proc. 1999 Intl. Stellarator Workshop, Madison, 1999), CD-ROM file P2-4 (2000).
[4] ICHIGUCHI, K., et al., Nucl. Fusion **41** (2001) 181.
[5] CARRERAS, B.A., et al., Phys. Plasmas **8** (2001) 990.
[6] NAKAMURA, Y., et al., J. Comp. Phys. **128** (1996) 43.
[7] GARCIA, L., et al., J. Comp. Phys. **65** (1986) 253.
[8] HIRSHMAN, S.P., et al., Comp. Phys. Comm. **43** (1986) 143.
[9] ICHIGUCHI, K., et al., Nucl. Fusion **36** (1996) 1157.
[10] LIANG, Y., et al., Plasma Phys. Control. Fusion **44** (2002) 1383.
[11] JOHNSON, J.L., and GREEN, J.M., Plasma. Phys. **9** (1967) 611.
[12] WAKATANI, M. et al., Nucl. Fusion **24** (1984) 1407.